Ceramics International 49 (2023) 37793–37799

Contents lists available at ScienceDirect

Ceramics International

journal homepage: www.elsevier.com/locate/ceramint

Significant reduction in processing time for $Ca_{0.95}Ce_{0.05}MnO_3$ thermoelectric ceramics

A. Sotelo [a,*], P. Amirkhizi [b], O.J. Dura [c], G. García [d], A.C. Asensio [d], M.A. Torres [a], M.A. Madre [a], A. Kovalevsky [b], Sh Rasekh [b]

[a] INMA (CSIC-Universidad de Zaragoza), M[a] de Luna, 3, 50018, Zaragoza, Spain
[b] Department of Materials and Ceramic Engineering, CICECO-Aveiro Institute of Materials, University of Aveiro, 3810-193, Aveiro, Portugal
[c] Applied Physics Department, University of Castilla-La Mancha, 13071, Ciudad Real, Spain
[d] Centro Stirling S. Coop, Av. Alava, 3, 20550, Aretxabaleta, Spain

ARTICLE INFO

Handling Editor: Dr P. Vincenzini

Keywords:
Milling
Electrical conductivity
Thermal conductivity
Transition metal oxides

ABSTRACT

Attrition-milling process has been applied to Ce-doped $CaMnO_3$ precursors to obtain small grain-size powders. The use of Ce^{4+} as dopant instead a Rare Earth^{3+} has allowed decreasing by 50% the atomic proportion of dopant, to obtain equivalent charge carrier concentration, which is required for attaining promising properties for thermoelectric applications. An impressive decrease in thermal processing time was achieved, together with an increase in thermoelectric performances, when compared to classically prepared materials. XRD and SEM analysis have confirmed that the final material is nearly single phase. Moreover, grain sizes and density increase with the sintering duration. These microstructural differences are reflected in a significant decrease in electrical resistivity, when compared to the samples prepared from ball-milled precursors (used as reference), without drastically modifying the Seebeck coefficient values. On the other hand, despite of their high electrical conductivity, thermal conductivity is decreased for short time sintered materials, leading to the highest ZT values at 800 °C (~0.27) in samples sintered for 1 h at 1310 °C. These values are among the best reported in the literature, but they have been obtained in very short time using a simple, and easily scalable process. The suggested approach presented in this work appears particularly promising for large-scale production of oxide-based thermoelectric modules for power generation.

1. Introduction

Today, one of humanity's main concerns is focused on reducing the use of fossil fuels and, therefore, the emission of greenhouse gases. In order to decrease these emissions, renewable energies (photovoltaic, thermal solar, wind, etc.) are being massively exploited throughout the world. On the other hand, all these renewable energy sources are not enough to fulfil the energetic requirements of society. Consequently, fossil fuels are still necessary in many sectors, even if their energetic efficiency is relatively low, loosing huge amounts of energy in the form of heat. In this scenario, thermoelectric (TE) power generation technologies are very promising, as they can be incorporated into the existing thermodynamic processes, increasing their overall efficiency. These devices can harvest energy from waste heat and/or natural heat sources [1,2] to produce useful electrical power. However, for these practical applications, it is necessary to produce TE materials with high energy conversion efficiency, which is quantified using the dimensionless figure of merit ZT, defined as $TS^2/\rho\kappa$ (S^2/ρ is also known as power factor, PF), where S is Seebeck coefficient, ρ electrical resistivity, κ thermal conductivity, and T absolute working temperature [3]. When analysing this expression, it is evident that high efficiency TE materials should have a high Seebeck coefficient, as well as low electrical resistivity and thermal conductivity.

Nowadays, commercial modules are based on semiconducting and intermetallic materials, which are usually composed of heavy and/or toxic elements. Moreover, they can melt, evaporate or oxidize at high temperatures under air, limiting their niche of applications. On the other hand, ceramic materials are deeply studied since the discovery of thermoelectric properties in Na_xCoO_2 [4], composed of less-toxic, more abundant and cheaper elements than the classical ones [5,6]. Furthermore, they can operate at higher temperatures than the classical thermoelectrics, under air, for a long time without oxidation and/or

* Corresponding author. Universidad de Zaragoza, Dept. Ciencia de Materiales, C/M[a] de Luna, 3, 50018, Zaragoza, Spain.
E-mail address: asotelo@unizar.es (A. Sotelo).

https://doi.org/10.1016/j.ceramint.2023.09.107
Received 9 June 2023; Received in revised form 19 August 2023; Accepted 11 September 2023
Available online 12 September 2023

evaporation. These works led to the discovery of new p-type compounds, such as $Ca_3Co_4O_9$ [7], with promising properties to be used in thermoelectric modules. However, for building these thermoelectric modules, it is necessary to prepare n-type ceramics counterpart, such as manganite or titanate-based compounds with similar properties [8,9]. Among these families, the most promising is $CaMnO_3$ due to its simple preparation under air atmosphere. Nevertheless, the pristine compound displays too high electrical resistivity due to its low charge carrier concentration ($7.1\ 10^{18}$–$1.02\ 10^{19}$ cm^{-3}) [10,11]. Consequently, it is necessary increasing this concentration to enhance its thermoelectric performances. It has been reported that 10 mol% substitution of Ca by trivalent elements maximizes these performances [12,13], increasing the charge carrier concentration up to $1.9\ 10^{21}$ cm^{-3} [14]. On the other hand, bulk compounds are produced through the classical solid-state method, involving several mixing, milling and thermal treatment processes. Nevertheless, this method typically leads to incomplete reactions and/or compositional inhomogeneities. These drawbacks, together with the increase in the materials production costs, due to the long preparation process and the use of expensive rare earth elements, make these materials less attractive for massive applications.

Additionally, it has been previously reported that preparation techniques may influence the final properties of bulk materials [15]. Consequently, the objective of this work is to reduce the costs of the raw materials, as well as those associated to the materials processing. Taking into account these limitations, Ce was used as a dopant, due to its lower cost, when compared to other RE. Moreover, it provides the possibility of using lower dopant concentration (5 mol%), as it displays +4 oxidation state, supplying 2 electrons to reach charge carrier concentrations of around $1.9\ 10^{21}$ cm^{-3}, which corresponds to that obtained with 10 mol% of a trivalent dopant [14]. Furthermore, attrition-milling was used to decrease particle size of initial precursors, which increase their reactivity, and allows reducing the thermal treatments duration. The structural and microstructural characteristics were evaluated and related to the thermoelectric properties of the final product. Furthermore, their performances were compared to the samples prepared through the classical solid-state method.

2. Experimental

The initial $Ca_{0.95}Ce_{0.05}MnO_3$ mixtures were prepared using $CaCO_3$ (≥99%, Aldrich), CeO_2 (99.9%, Aldrich), and Mn_2O_3 (99.9%, Aldrich) commercial powders. They were weighed in stoichiometric proportions and well mixed. The milling procedure was different for both types of samples: classically prepared materials were first ball-milled in an agate ball-mill at 300 rpm for 2 h in water media, while the attrition-milled precursors were ground in an attrition-mill with zirconia balls at 400 rpm for 2 h in water media. The attrition-milling process consists in a Teflon cylindrical container where the precursor powders are introduced with a large number of 1 mm diameter zirconia balls and water. Once the mixture has been prepared, and agitator, consisting in three blades at different heights and distributed at 120°, is rotated to grind the precursors due to the friction between the balls and the precursor powders. The two different suspensions were then totally dried under IR radiation, followed by manual milling to produce brownish-fine powders. The precursors for the classical solid state method were thermally treated using a two-step procedure, at 950 °C for 12 h, and 1050 °C for 12 h with an intermediate milling. It should be highlighted that the best conditions found experimentally for the calcination of attrition-milled precursors were at 1100 °C for 1 h. For this purpose, attrition-milled calcined powders in different conditions were analysed through FTIR spectrometry until reaching the same spectrum obtained in the ball-milled precursors after calcination. After the calcination procedure, powders were cold uniaxially pressed under 400 MPa in the form of pellets and sintered at 1310 °C for 12 h for the solid-state method and for 1, 3, 6, and 12 h for the attrition-milled precursors.

Powder X-ray diffraction (XRD) has been performed using a Rigaku Ru300 between 5 and 60° to identify the phases in the samples. Density measurements have been performed using Archimedes' method on several samples for each processing condition, using 4.705 g/cm^3 as a reference for the theoretical density [16]. Microstructural studies were performed on the precursor powders after each step, and on samples surfaces after sintering using a FESEM (Zeiss Merlin) equipped with an energy dispersive spectrometer (EDS) to determine the elemental composition of grains. Moreover, grain sizes were estimated by performing the image analysis for the powders, and using the line intercept method on sintered materials [17]. FTIR spectrometry has been carried out in a Bruker IFS 28 Spectrometer on the samples after each thermal treatment, using the spectrum of the mixed precursor powders as reference.

Electrical resistivity and Seebeck coefficient were simultaneously measured in steady state mode, using the standard DC four-probe technique, in an LSR-3 apparatus (Linseis GmbH) between 50 and 800 °C under He atmosphere. Thermal diffusivity (α) has been measured in the same direction used for the electrical characterization in a laser-flash system (Linseis LFA 1000). Thermal conductivity (κ) has been calculated as $\kappa = \alpha\ C_p\ d$, being C_p specific heat and d, sample density. C_p has been calculated using Dulong-Petit law. As it is well known, thermal conductivity is composed of two contributions, the electronic and the phononic (or lattice) ones, in the form $\kappa = \kappa_{el} + \kappa_{ph}$. κ_{el} can be calculated using the Wiedemann-Franz law, as $\kappa_{el} = L\ \sigma\ T$, where L is Lorenz number, σ electrical conductivity, and T absolute temperature. Moreover, in order to determine and compare the TE performances, ZT was calculated from Seebeck coefficient, electrical resistivity, and thermal conductivity data. These data were used to evaluate the evolution of the properties as a function of the sintering time, and were also compared with previously reported values in the literature for similar compounds.

3. Results and discussion

Representative SEM micrographs of precursor powders are shown in Fig. 1, after ball-and attrition-milling (a, and b, respectively) and calcination procedure of ball- and attrition-milled precursors (c, and d, respectively). As it can be easily observed in these micrographs, the particle sizes seem to be much smaller after attrition-milling when compared to those produced through ball-milling. Moreover, by comparing the particle sizes after the calcination procedure, this trend is more evident. In order to evaluate these changes in size after each processing step, grain sizes were determined using image analysis, and the results are presented in Table 1. As it is shown in the table, grain sizes are increasing with the calcination procedure being, at least, three times larger for the ball-milled precursors than for the attrition-milled ones. This effect is due to the larger calcination process in the former case, despite of its lower temperatures. However, in both cases, the increase in grain sizes is about three times from the milled precursors to the calcined ones. Taking into account the calcination conditions for both types of precursors, the higher reactivity of attrition-milled precursors is due to their much smaller particle sizes after milling when compared to the ball-milled ones.

Fig. 2 presents the FTIR spectra of initial powders and after calcination for both milling processes. As it can be easily observed in the graph, the $CaCO_3$, CeO_2, and Mn_2O_3 mixture (denoted as precursors) shows only the typical absorbance peaks of $CaCO_3$ (a strong one between 1450–1400 and a medium one at 880-880 cm^{-1} [18]) in the studied 1800-800 cm^{-1} region. After calcining the ball-milled powders at 950 °C for 12 h, some calcium carbonate is still present in the samples, disappearing (or being below the detection limit of the technique) after the second calcination step at 1050 °C. On the other hand, attrition-milled samples reach the same situation (no $CaCO_3$ detected) after only 1 h at 1100 °C. This fact is due to the microstructural features previously described, which enhance the particles reactivity and the diffusion rates.

Powder XRD patterns for all samples are presented (from 10 to 50° for clarity) in Fig. 3. As it can be observed in the graph, all samples

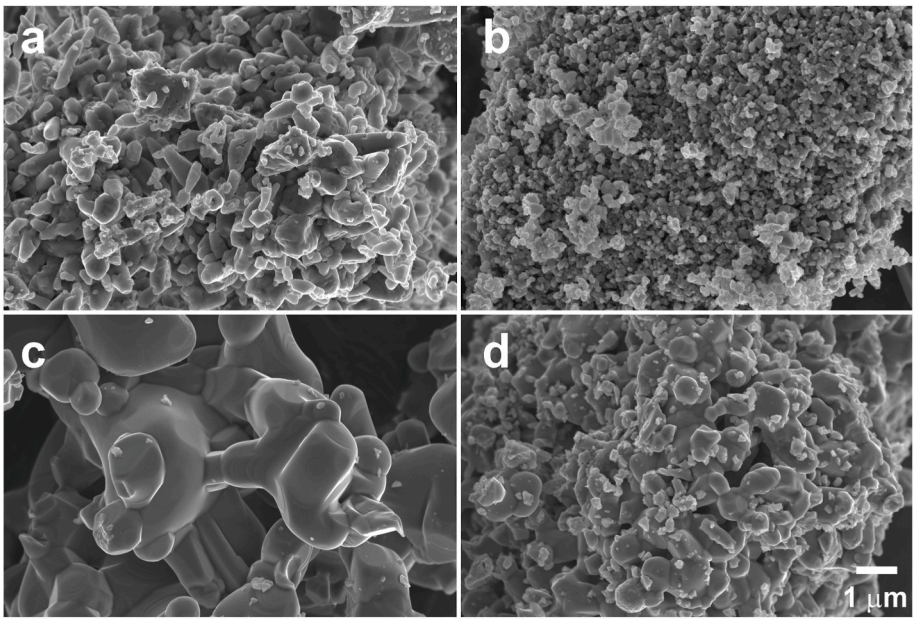

Fig. 1. SEM micrographs of precursor powders after a) ball; and b) attrition-milling, and after calcination c) 950 °C for 12 h and 1050 °C 12 h ball-milled precursors; and d) 1100 °C 1 h attrition-milled precursors.

Table 1
Mean grain size of samples, together with their standard deviation, after each processing step.

	As milled	Calcined 950 °C 12 h	Calcined 1050 °C 12 h	Calcined 1100 °C 1 h	Sintered 1310 °C 1 h	Sintered 1310 °C 3 h	Sintered 1310 °C 6 h	Sintered 1310 °C 12 h
Attrition milled	163 ± 72 nm	–	–	490 ± 288 nm	3.7 ± 0.2 μm	4.9 ± 0.4 μm	6.1 ± 1.0 μm	8.3 ± 0.8 μm
Ball milled	441 ± 289 nm	601 ± 316 nm	1466 ± 866 nm	–	–	–	–	6.5 ± 0.8 μm

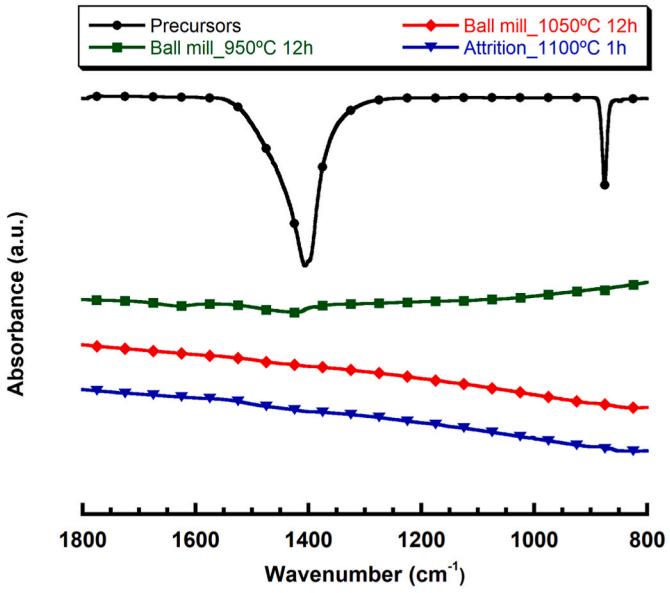

Fig. 2. FTIR spectra obtained in the different samples performed on the region where the CaCO3 compound shows its highest absorbance.

display the same pattern, and all the peaks can be associated to the crystallographic planes of $CaMnO_3$ phase with a *Pnma* space group (JCPDS card No. 04-008-4530), in agreement with previously reported data [19]. These results clearly show that all samples are single-phase and that the processing conditions are adequate to produce the thermoelectric phase.

Fig. 4 presents representative SEM micrographs performed on the surfaces of samples produced from both types of precursors and sintered at 1310 °C for different times. The images show a larger amount of porosity in the samples produced from ball-milled precursors sintered for 12 h than for attrition-milled ones, independently of the sintering duration (compare Fig. 4a–. 4b, c, and d). Moreover, grain sizes are increased, and porosity is decreased in samples produced from attrition-milled precursors when the sintering time is raised. The evolution of grain sizes as a function of precursors and the sintering time has been evaluated through the line-intercept method using several micrographs for each sintering conditions. The obtained results, together with their standard deviation are shown in Table 1. As it can be observed in the table, in spite of the very small particle sizes obtained after calcining the attrition-milled precursors, their high reactivity leads to a rapid increase of grain sizes during the sintering procedure. Furthermore, after 12 h sintering, these grains are about 25% larger than the obtained in samples produced from ball-milled precursors sintered in the same conditions. On the other hand, EDS analysis performed in several regions of each sample has revealed that the mean composition corresponds to the nominal composition, with a very slight Ca deficiency in all cases. These EDS results clearly confirm the XRD data discussed previously, and the substitution of Ca by Ce, in agreement with previous studies [8].

As mentioned, SEM micrographs seem to show a decrease in porosity from the ball-milled to the attrition-milled precursors. Moreover, porosity is further decreased when the sintering time is increased. These observations were corroborated through absolute density measurements, illustrated in Table 2. As it can be observed, the density follows the trends suggested through the SEM images. These values correspond

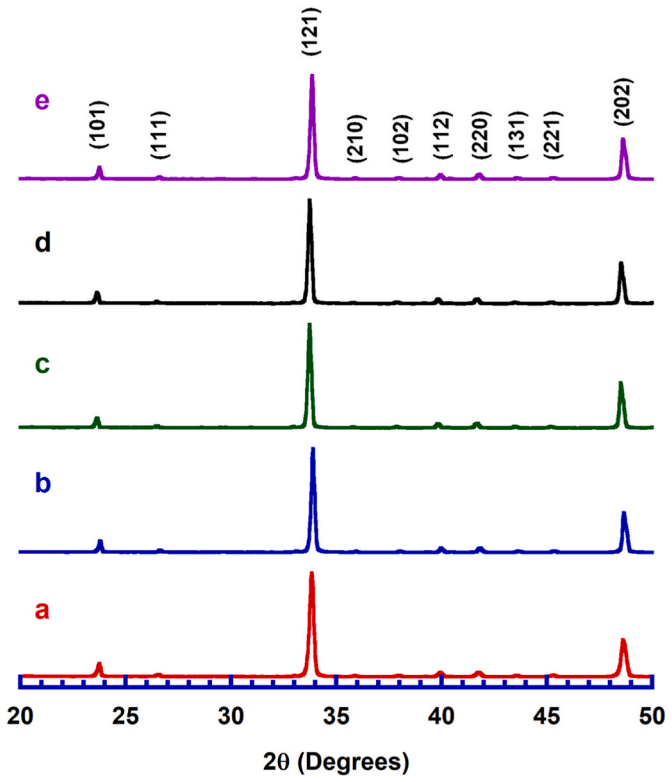

Fig. 3. Powder XRD patters obtained in the different samples after sintering at 1310 °C. a) ball-milled and sintered for 12 h; and attrition-milled and sintered for b) 1; c) 6; and d) 12 h.

to relative densities between 89 and 94% of the theoretical density of $CaMnO_3$ [16], which are much higher than the typically obtained in sintered materials (76–79%) [11,20].

The temperature dependence of the electrical resistivity is shown in Fig. 5 for all samples, together with some values from different literature sources. All the samples present metallic-like behaviour ($d\rho/dT > 0$) in the whole measured temperature range. Moreover, samples produced from attrition-milled precursors display lower resistivity than those obtained from ball-milled ones, due to their larger density. However, the differences between the attrition-milled samples are significant only for those sintered for 1 h, when compared to those sintered for longer time, as the density differences are very small. The decrease in electrical resistivity with sintering time in the attrition-milled samples is due to the grain growth induced by the sintering duration (see Table 1), decreasing the number of grain boundaries, which are more resistive than the intragrain regions. The lowest electrical resistivity at 800 °C (5.8 mΩ cm) has been determined in attrition-milled samples sintered for more than 1 h, which is about 15% lower than the measured in ball-milled samples, and close to the reported in Pr and Sr co-doped $CaMnO_3$ prepared by sol-gel method (~5.5 mΩ cm) [21]. Furthermore, this value is much lower than those presented in the literature for laser grown samples (9 mΩ cm) [22], or electronically doped materials (9–22 mΩ cm) [13,23–25]. It is worth mentioning that all these reported values in the literature have been achieved using longer and/or more complex processes.

Fig. 6 displays the variation of the Seebeck coefficient as a function of temperature for all samples, as well as data from literature. All samples exhibit negative values in the whole studied temperature range, confirming that the electrical conduction mechanism is dominated by electrons. Furthermore, the |S| values are increasing with temperature in all samples, which is associated with the behaviour of a metal or degenerated semiconductor when the variation of carrier concentration, effective mass, and Fermi level with temperature are negligible [26]. Consequently, all samples display, approximately, the same |S| values due to the fact that they have the same composition and the same charge carrier concentration. Moreover, even if some variation could be

Table 2
Absolute density determined through Archimedes' method for all sintered samples together with their standard deviation.

	Density (g/cm^3)	Standard deviation
Ball milled 1310°C 12h	4.17	0.08
Attrition milled 1310°C 1h	4.34	0.03
Attrition milled 1310°C 3h	4.35	0.02
Attrition milled 1310°C 6h	4.37	0.04
Attrition milled 1310°C 12h	4.41	0.03

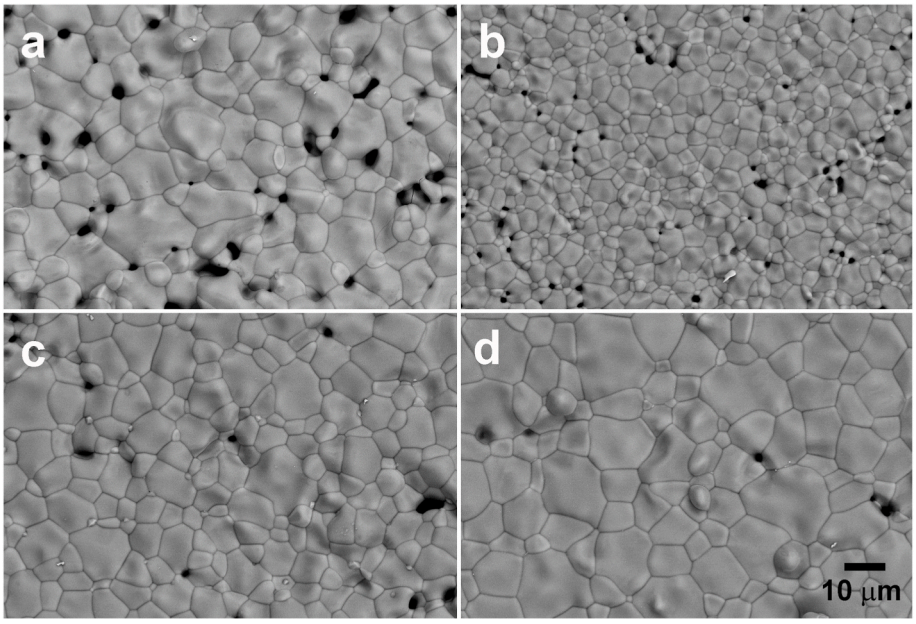

Fig. 4. Representative SEM micrographs performed on the surfaces of sintered samples. a) ball-milled precursors sintered at 1310 °C for 12 h; and attrition-milled precursors sintered at 1310 °C for b) 1 h; c) 6 h; and d) 12 h.

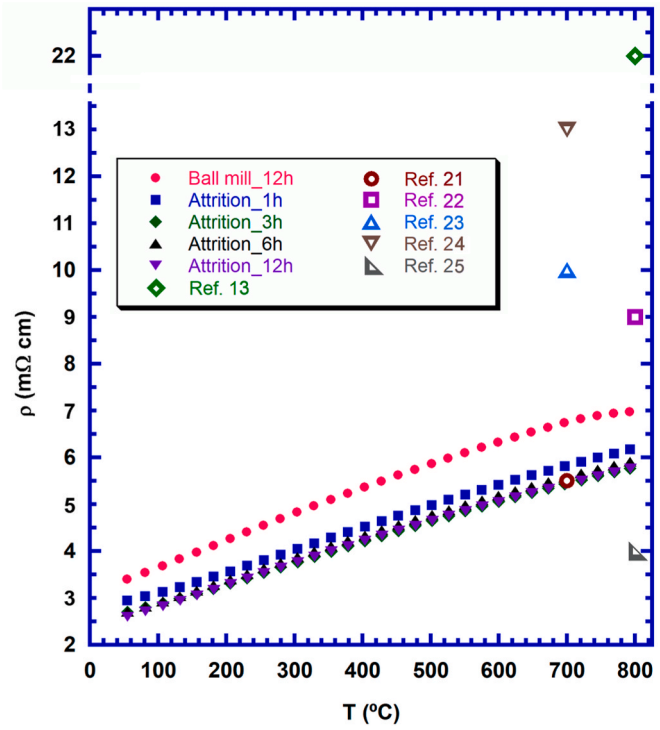

Fig. 5. Temperature dependence of the electrical resistivity for all samples, together with data extracted from the literature.

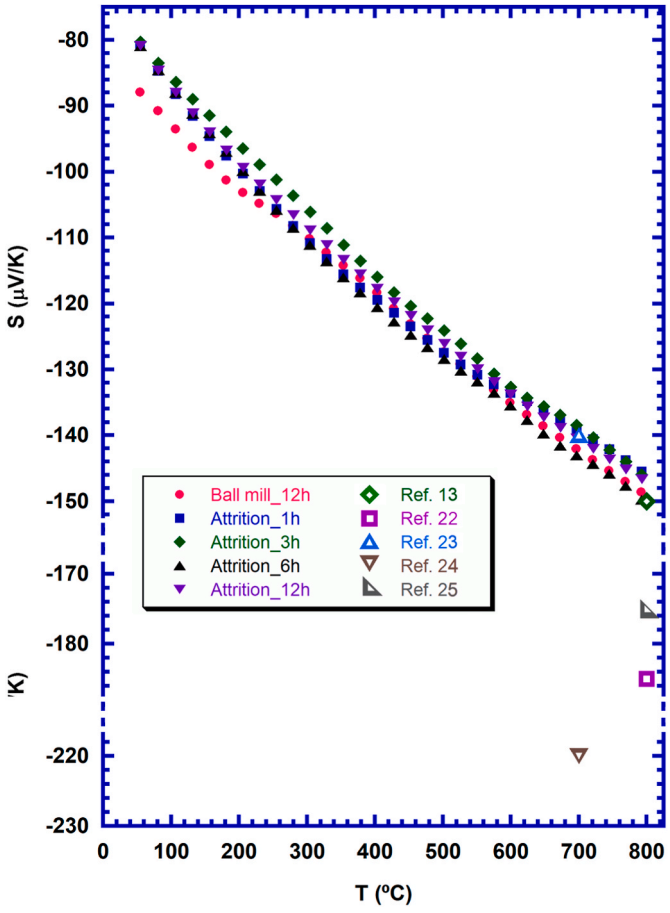

Fig. 6. Temperature dependence of the Seebeck coefficient for all samples, together with data extracted from the literature.

expected due to the microstructural modifications, it is well known that Seebeck coefficient is much less sensitive to these changes than electrical resistivity, explaining its very small variation between the samples. The highest |S| value at 800 °C (150 μV/K), which is in the order of the best compositions presented in the literature for doped compounds (140–160 μV/K) [13,22–25].

Using the electrical resistivity and Seebeck coefficient values, PF has been calculated for all the samples (graph not shown), reaching the highest value for the attrition-milled samples sintered at 800 °C for 3, 6, and 12 h (~0.38 mW/K^{2}m), which is about 20% higher than the obtained in ball-milled samples (~0.32 mW/K^{2}m). Moreover, it is much higher than those reported for doped materials (0.1–0.2 mW/K^{2}m) [13,23,24], and it is in the order of those produced using longer and more complicated processes (0.36–0.40 mW/K^{2}m) [21,22,25]. In spite of the short thermal treatment processes used for the attrition-milled precursors, these results clearly illustrate their high reactivity and the good grains connectivity produced in these materials, leading to high electrical performances.

Fig. 7 presents the total and the lattice thermal conductivity evolution with temperature for all samples, and the values reported in the literature. As shown in Fig. 7a, κ is increasing with the sintering time in attrition-milled samples in the whole measured temperature range. This evolution is in agreement with the grain size and density changes previously discussed for these samples, leading to higher thermal conductivities when density is increased and lower number of grain boundaries are attained due to the grain growth. On the other hand, the values for the ball-milled ones are approximately the same as obtained for the attrition-milled-samples sintered for 3 h. Another interesting observation in the graph, is that κ decreases with temperature up to around 500 °C, increasing for higher temperatures. This behaviour reflects the complex interrelationship of different contributions. Firstly, from room temperature the lattice thermal conductivity decreases as temperature rise due to the Umklapp phonon-phonon scattering (T^{-1}). However, at higher temperatures other mechanisms competes/participates as the scattering due defects or boundaries among others [27]. At the highest temperatures the clear rise of kappa with temperature would reflects a bipolar contribution to thermal conductivity [27]. This contribution is not quite evident from the Seebeck coefficient dependence, however a sight change of the slope (S(T) vs. T) can be inferred at the temperature where the change in kappa is evident. The lowest κ at 800 °C has been measured in attrition-milled samples sintered for 1 h (1.35 W/K m), which is around 20% lower than the measured for ball-milled ones due to the higher number of grain boundaries which, in turn, enhance phonon scattering. Furthermore, it is much lower than those reported for electronically doped materials (1.40–3.60 W/K m) [8,11,12,21,25,28]. However, it is still higher than that reported for multiple substituted $CaMnO_3$ compound (1.24 W/K m) [29] due to its higher number and amount of dopants. Moreover, despite the larger contribution of the electronic thermal conductivity to the total thermal conductivity in attrition-milled samples, lattice thermal conductivity presents the same evolution as the total one for all samples. Consequently, it is clear that in attrition-milled samples, the lattice thermal conductivity contribution to κ is decreased when the sintering time is decreased. This fact can be associated to a lower reaction time, which could result in an increase of intragrain stresses produced by the presence of $CaMnO_3$ and $CaMn_2O_4$-type structures inside the grains, as reported in Ref. [29], due to the lower reaction times. However, as it can be observed in the graph, thermal conductivity does not show a continuous decreasing trend with temperature, as it increases at T > 500 °C. This behaviour is due to the high electronic thermal conductivity contribution at these temperatures.

Finally, with the electrical resistivity, Seebeck coefficient, and total thermal conductivity data, ZT has been calculated, and presented in Fig. 8, as a function of temperature, for all samples, and compared to the typical values reported in the literature. As it can be observed in the graph, the highest values have been achieved in the attrition-samples sintered for just 1 h, provided by their very low thermal conductivity.

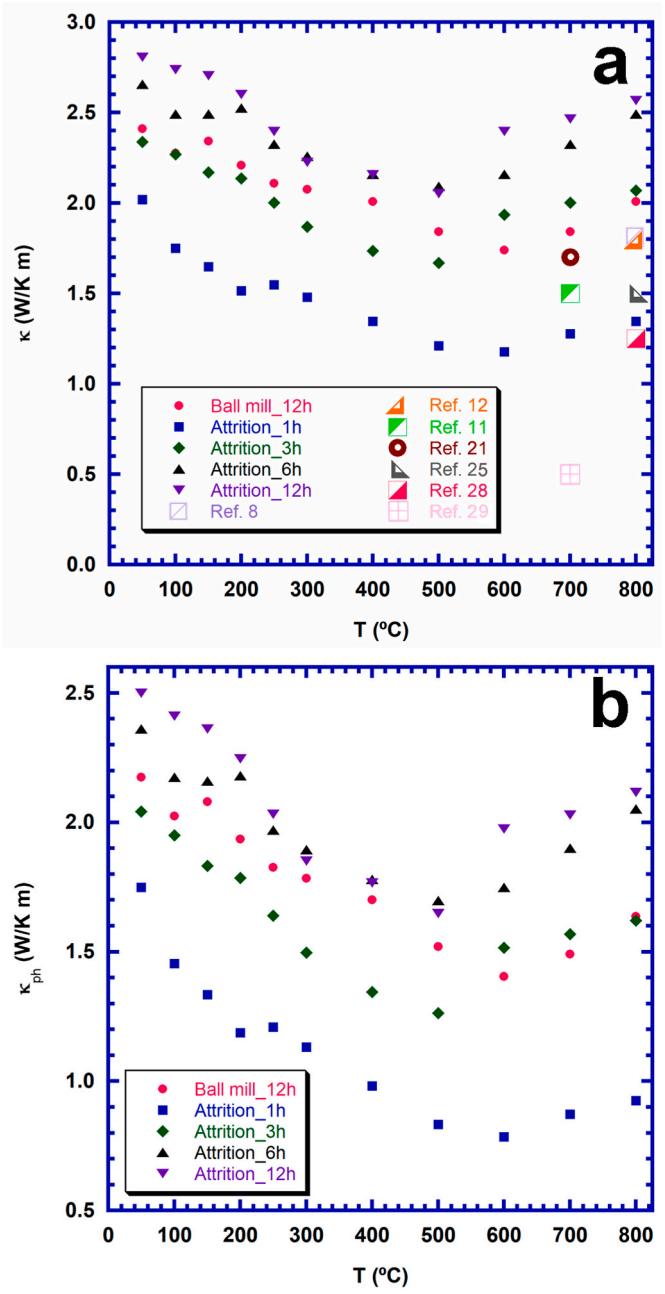

Fig. 7. Temperature dependence of the total thermal conductivity (a); and lattice thermal conductivity (b) for all samples, together with total thermal conductivity data extracted from the literature.

On the other hand, the other samples display very similar ZT values in the whole measured temperature range. The highest ZT value at 800 °C (~0.27) in samples sintered for 1 h is around 40% higher than for the other samples in this work. Moreover, this value is among the best reported ones in the literature (0.08–0.29) [8,11,25,28–33] for samples produced using longer and more complex procedures, including more expensive and higher amount of dopants.

It should be highlighted that these high ZT values have been obtained combining a relatively cheap dopant in amounts 50% lower than usually due to its +4 oxidation state, with attrition-milling process and a very short thermal treatment. These characteristics make these sintered materials promising candidates for practical applications in high-temperature thermoelectric devices.

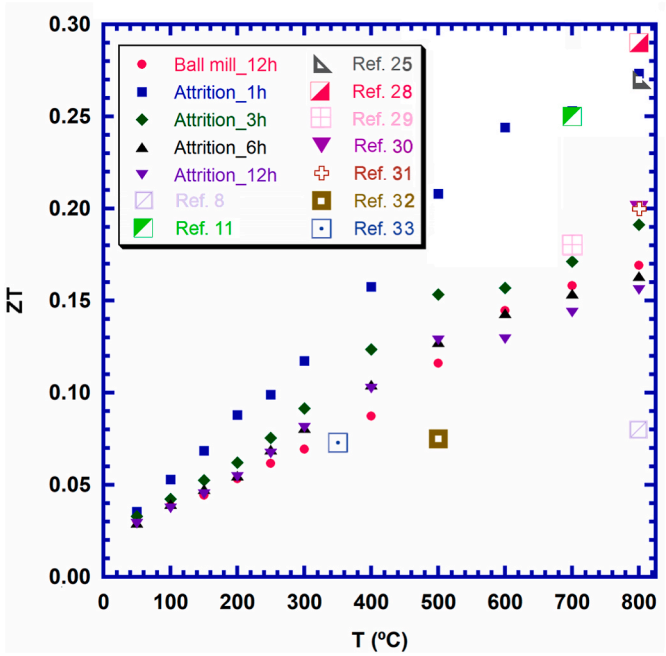

Fig. 8. Temperature dependence of ZT for all samples, together with data extracted from the literature.

4. Conclusions

In this work, the prospects for using a relatively low-cost rare earth element with a +4 oxidation state as a dopant for $CaMnO_3$ was studied, seeking an appropriate thermoelectric performance. Moreover, it allows using lower amount of the dopant, as compared to +3 rare earths. Additionally, attrition-milling has been applied on the precursors to reduce their starting particle sizes and decrease the thermal treatment duration provided by their higher reactivity when compared to ball-milled precursors with the same composition. Consequently, the calcination procedure has been reduced to 1 h at 1100 °C for the attrition-milled samples, while a longer procedure, including calcinations at 950 °C for 12 h, followed by 1050 °C for 12 h, was required to produce similar precursors in the ball-milled products. Sintering at 1310 °C for 12 h was involved in the case of precursors obtained by ball-milling, while 1, 3, 6, and 12 h were applied on the attrition-milled ones for comparison. XRD patterns have shown the formation of Ce doped $CaMnO_3$ phase in all cases, confirming the high reactivity of attrition-milled powders. Microstructural studies indicated that grain sizes are increased and porosity decreased with the sintering duration. Furthermore, higher densities have been achieved for samples produced from attrition-milled precursors, when compared to ball-milled ones. All these features are reflected in a significant decrease in electrical resistivity of these samples when compared to those obtained from ball-milled precursors, while Seebeck coefficient has been maintained unchanged due to the same Ce substitution. On the other hand, thermal conductivity is significantly decreased in samples sintered for 1 h, leading to the highest ZT values in the whole measured temperature range, when compared to the other samples in this work. The highest ZT calculated value at 800 °C is among the best reported in the literature, but it was reached using a lower-cost dopant, its lower amount, and relatively short thermal treatments. Thus, such an approach is promising for large-scale production of the $CaMnO_3$-based materials for energy harvesting applications.

Declaration of competing interest

The authors declare that they have no known competing financial

interests or personal relationships that could influence the work reported in this paper.

Acknowledgements

The authors wish to thank the Gobierno de Aragón (Grupo de Investigacion T54_23R) and Universidad de Zaragoza (UZ2022-IAR-09) for financial support. G. García and A. C. Asensio acknowledge the Basque Government Industry Department through the Elkartek program (Exp: KK-2022/00040 - DIFERENTE). Sh. Rasekh acknowledges the support of the Research Employment Contract FCT–CEECIND/02608/2017. This work was also developed within the scope of the PhD project of P. Amirkhizi (grant 2020.08051. BD funded by FCT) and the project CICECO-Aveiro Institute of Materials, UIDB/50011/2020, UIDP/50011/2020 & LA/P/0006/2020, financed by national funds through the FCT/MCTES (PIDDAC). Authors would like to acknowledge the use of Servicio General de Apoyo a la Investigación-SAI, Universidad de Zaragoza.

References

[1] A.E. Risseh, H.P. Nee, O. Erlandsson, K. Brinkfeldt, A. Contet, F.F. Lng, G. Gaiser, A. Saramat, A. Saramat, T. Skare, S. Nee, J. Dellrud, Design of a thermoelectric generator for waste heat recovery application on a drivable heavy duty vehicle, SAE Int. J. Commer. Veh. 10 (2017) 26–44, https://doi.org/10.4271/2017-01-9178.

[2] L. Catalan, P. Alegria, M. Araiz, D. Astrain, Field test of a geothermal thermoelectric generator without moving parts on the Hot Dry Rock field of Timanfaya National Park, Appl. Therm. Eng. 222 (2023), 119843, https://doi.org/10.1016/j.applthermaleng.2022.119843.

[3] D.M. Rowe, in: D.M. Rowe (Ed.), Thermoelectrics Handbook: Macro to Nano, CRC Press, Boca Raton, 2006.

[4] I. Terasaki, Y. Sasago, K. Uchinokura, Large thermoelectric power in $NaCo_2O_4$ single crystals, Phys. Rev. B 56 (1997) 12685–12687, https://doi.org/10.1103/PhysRevB.56.R12685.

[5] A.A. Yaroshevsky, Abundances of chemical elements in the earth's crust, Geochem. Int. 44 (2006) 48–55, https://doi.org/10.1134/S001670290601006X.

[6] S. LeBlanc, Thermoelectric generators: linking material properties and systems engineering for waste heat recovery applications, Sust. Mater. Technol. 1–2 (2014) 26–35, https://doi.org/10.1016/j.susmat.2014.11.002.

[7] A.C. Masset, C. Michel, A. Maignan, M. Hervieu, O. Toulemonde, F. Studer, B. Raveau, J. Hejtmanek, Misfit-layered cobaltite with an anisotropic giant magnetoresistance: $Ca_3Co_4O_9$, Phys. Rev. B 62 (2000) 166–175, https://doi.org/10.1103/PhysRevB.62.166.

[8] M. Ohtaki, H. Koga, T. Tokunaga, K. Eguchi, H. Arai, Electrical transport properties and high-temperature thermoelectric performance of $(Ca_{0.9}M_{0.1})MnO_3$ (M= Y, La, Ce, Sm, In, Sn, Sb, Pb, Bi), J. Solid State Chem. 120 (1995) 105–111, https://doi.org/10.1006/jssc.1995.1384.

[9] Y. Mune, H. Ohta, K. Koumoto, T. Mizoguchi, Y. Ikuhara, Enhanced Seebeck coefficient of quantum-confined electrons in $SrTiO_3/SrTi_{0.8}Nb_{0.2}O_3$ superlattices, Appl. Phys. Lett. 91 (2007), 192105, https://doi.org/10.1063/1.2809364.

[10] K. Fujimoto, M. Gibu, Y. Yamaguchi, A. Aimi, K. Nishio, O. Rabin, I. Takeuchi, Thermoelectric properties of bismuth-substituted calcium manganite $Ca_{1-x}Bi_xMnO_{3-\delta}$ prepared via the electrostatic spray deposition method, J. Ceram. Soc. Jpn. 125 (2017) 308–312, https://doi.org/10.2109/jcersj2.16277.

[11] R. Kabir, R. Tian, T. Zhang, R. Donelson, T.T. Tan, S. Li, Role of Bi doping in thermoelectric properties of $CaMnO_3$, J. Alloy Compd. 628 (2015) 347–351, https://doi.org/10.1016/j.jallcom.2014.12.141.

[12] T. Wang, P. Nan, H.C. Wang, W. Su, A. Sotelo, J. Zhai, X. Wang, Y. Ran, T. Chen, C. L. Wang, Right heterogeneous microstructure for achieving excellent thermoelectric performance in $Ca_{0.9}R_{0.1}MnO_{3-\delta}$ (R=Dy, Yb) ceramics, Inorg. Chem. 57 (2018) 9133–9141, https://doi.org/10.1021/acs.inorgchem.8b01163.

[13] D. Flahaut, T. Mihara, R. Funahashi, N. Nabeshima, K. Lee, H. Ohta, K. Koumoto, Thermoelectrical properties of A-site substituted $Ca_{1-x}Re_xMnO_3$ system, J. Appl. Phys. 100 (2006), 084911, https://doi.org/10.1063/1.2362922.

[14] T. Yang, T. Cheng, Effects of La, Sm and Yb doping on thermoelectric properties of $Ca_{0.98}Er_{0.02}MnO_3$ at high temperature, RSC Adv. 7 (2017) 44659–44664, https://doi.org/10.1039/c7ra08446c.

[15] A. Sotelo, M.A. Madre, M.A. Torres, J.C. Diez, Effect of synthesis process on the densification, microstructure, and electrical properties of $Ca_{0.9}Yb_{0.1}MnO_3$ ceramics, Int. J. Appl. Ceram. Technol. 14 (2017) 1190–1196, https://doi.org/10.1111/ijac.12711.

[16] R. Lohnert, M. Stelter, J. Topfer, Evaluation of soft chemistry methods to synthesize Gd-doped $CaMnO_{3-\delta}$ with improved thermoelectric properties, Mater. Sci. Eng. B 223 (2017) 185–193, https://doi.org/10.1016/j.mseb.2017.06.014.

[17] E. Heyn, Short reports from the metallurgical and metallographical laboratory of the royal mechanical and technical testing Institute of charlottenburg, The Metallographist 5 (1903) 39–64.

[18] NIST Chemistry WebBook. http://webbook.nist.gov/chemistry/.

[19] K.R. Poeppelmeier, M.E. Leonowicz, J.C. Scanlon, J.M. Longo, W.B. Yelon, Structure determination of $CaMnO_3$ and $CaMnO_{2.5}$ by X-ray and neutron methods, J. Solid State Chem. 45 (1982) 71–79, https://doi.org/10.1016/0022-4596(82)90292-4.

[20] A. Sotelo, M.A. Torres, M.A. Madre, J.C. Diez, Role of Ag on the properties of $Ca_{0.9}Yb_{0.1}MnO_3$ sintered ceramics, Materials 11 (2018) 2503, https://doi.org/10.3390/ma11122503.

[21] K.K. Liu, Z.Y. Liu, F.P. Zhang, J.X. Zhang, X.Y. Yang, J.W. Zhang, J.L. Shi, G. Ren, T.W. He, J.J. Duan, Improved thermoelectric performance in Pr and Sr Co-doped $CaMnO_3$ materials, J. Alloys Compd. 808 (2019), 151476, https://doi.org/10.1016/j.jallcom.2019.07.188.

[22] N.M. Ferreira, N.R. Neves, M.C. Ferro, M.A. Torres, M.A. Madre, F.M. Costa, A. Sotelo, A.V. Kovalevsky, Growth rate effects on the thermoelectric performance of $CaMnO_3$-based ceramics, J. Eur. Ceram. Soc. 39 (2019) 4184–4188, https://doi.org/10.1016/j.jeurceramsoc.2019.06.011.

[23] M. Mouyane, B. Itaalit, Flash Combustion Synthesis of electron doped-$CaMnO_3$ thermoelectric oxides, Powder Technol. 264 (2014) 71–77, https://doi.org/10.1016/j.powtec.2014.05.022.

[24] Y.C. Zhou, C.L. Wang, W.B. Su, J. Liu, H.C. Wang, J.C. Li, Y. Li, J.Z. Zhai, Y. C. Zhang, L.M. Mei, Electrical properties of Dy^{3+}/Na^+ Co-doped oxide thermoelectric $[Ca_{1-x}(Na_{1/2}Dy_{1/2})_x]MnO_3$ ceramics, J. Alloys Compd. 680 (2016) 129–132, https://doi.org/10.1016/j.jallcom.2016.04.158.

[25] Y.-H. Zhu, W.-B. Su, J. Liu, Y.-C. Zhou, J. Li, X. Zhang, Y. Du, C.-L. Wang, Effects of Dy and Yb co-doping on thermoelectric properties of $CaMnO_3$ ceramics, Ceram. Int. 41 (2015) 1535–1539, https://doi.org/10.1016/j.ceramint.2014.09.089.

[26] D. Flahaut, J. Allouche, A. Sotelo, Sh Rasekh, M.A. Torres, M.A. Madre, J.C. Diez, Role of Ag in textured-annealed $Bi_2Ca_2Co_{1.7}O_x$ thermoelectric ceramic, Acta Mater. 102 (2016) 273–283, https://doi.org/10.1016/j.actamat.2015.09.036.

[27] H. Geng, X. Meng, H. Zhang, J. Zhang, Lattice thermal conductivity of filled skutterudites: an anharmonicity perspective, J. Appl. Phys. 116 (2014), 163503, https://doi.org/10.1063/1.4898686.

[28] G. Xu, R. Funahashi, I. Matsubara, M. Shikano, Y. Zhou, High-temperature thermoelectric properties of the $Ca_{1-x}Bi_xMnO_3$ system, J. Mater. Res. 17 (2002) 1092–1095, https://doi.org/10.1557/JMR.2002.0161.

[29] M.A. Madre, H. Amaveda, O.J. Dura, D. Pelloquin, M. Mora, M.A. Torres, S. Marinel, A. Sotelo, Effect of Y, La, and Yb simultaneous doping on the thermal conductivity and thermoelectric performances of $CaMnO_3$ ceramics, J. Alloys Compd. 954 (2023), 170201, https://doi.org/10.1016/j.jallcom.2023.170201.

[30] T. Chen, J. Wang, X. Wang, H. Wang, W. Su, J. Zhai, F. Mehmood, M. Khan, C. Wang, Cross-scale porous structure design leads to optimized thermoelectric performance and high output power for $CaMnO_3$ ceramics and their uni-leg modules, Appl. Mater. Today 29 (2022), 101557, https://doi.org/10.1016/j.apmt.2022.101557.

[31] Y. Wang, Y. Sui, W.H. Su, High temperature thermoelectric characteristics of $Ca_{0.9}R_{0.1}MnO_3$ (R = La, Pr, …,Yb), J. Appl. Phys. 104 (2008), 093703, https://doi.org/10.1063/1.3003065.

[32] Y. Wang, Y. Sui, H. Fan, X. Wang, W. Su, X. Liu, High temperature thermoelectric response of electron-doped $CaMnO_3$, Chem. Mater. 21 (2009) 4653–4660, https://doi.org/10.1021/cm901766y.

[33] A. Bhaskar, C. Liu, J. Yuan, Thermoelectric and magnetic properties of $Ca_{0.98}Re_{0.02}MnO_{3-\delta}$ (Re=Sm, Gd and Dy), J. Electron. Mater. 41 (2012) 2338–2344, https://doi.org/10.1007/s11664-012-2159-6.